Revisiting the interplay between ablation, collisional, and radiative processes during ns-laser ablation

D. Autrique,[1,2,a)] I. Gornushkin,[3] V. Alexiades,[4] Z. Chen,[2,b)] A. Bogaerts,[2] and B. Rethfeld[1]
[1]*Department of Physics and OPTIMAS Research Center, TU Kaiserslautern, 67653 Kaiserslautern, Germany*
[2]*Department of Chemistry, University of Antwerp, 2610 Wilrijk, Belgium*
[3]*Federal Institute for Materials Research and Testing - BAM, 12489 Berlin, Germany*
[4]*Department of Mathematics, University of Tennessee, Knoxville, Tennessee 37996-1320, USA*

(Received 12 September 2013; accepted 7 October 2013; published online 21 October 2013)

A study of ns-laser ablation is presented, which focuses on the transient behavior of the physical processes that act in and above a copper sample. A dimensionless multiphase collisional radiative model describes the interplay between the ablation, collisional, and radiative mechanisms. Calculations are done for a 6 ns-Nd:YAG laser pulse operating at 532 nm and fluences up to 15 J/cm^2. Temporal intensity profiles as well as transmissivities are in good agreement with experimental results. It is found that volumetric ablation mechanisms and photo-processes both play an essential role in the onset of ns-laser induced breakdown. © *2013 AIP Publishing LLC*. [http://dx.doi.org/10.1063/1.4826505]

Nanosecond-laser ablation results in a variety of closely connected processes, acting above and beneath the sample surface such as melting, evaporation, plume expansion, and laser-induced breakdown. In the latter process, a hot plasma can be formed, which shields the target from the laser beam and reduces the amount of energy deposited in the sample.[1,2] Such feedback effects often thwart the experimental identification of the individual mechanisms. Contrary to experiments, theoretical models allow an independent study of the various processes.

An adequate description of ns-laser induced plasma formation requires a detailed knowledge of the temporal and spatial evolution of the bound and free electrons as well as the heavy species in the ablated material. In principle, this can only be achieved through a full kinetic description, in which all collisional and radiative processes occurring in the plasma are considered and resolved.[3–5] In the past, collisional-radiative models were introduced to handle this problem.[6–10] In such models, a set of rate equations attempts to resolve the various physical processes in the plasma on their characteristic time scale. Non-equilibrium studies of ns-laser induced breakdown in metal vapors at variable laser settings revealed the important role of photo-processes.[8,9] It was found that single[9] and multi-photon ionization[8] and resonant as well as non-resonant photo-excitation[9] play a predominant role during UV-VIS-laser induced breakdown.

In most of these models, however, surface evaporation was treated as the main ablation mechanism.[7,8] In the present work, it will be demonstrated that this picture is incomplete and results in a mismatch between experiment and theory. Surface evaporation implies that a clear phase boundary between the liquid and vapor phases exists and binodal relations hold. At sufficiently high laser irradiances, however, the sample will reach or exceed the critical temperature, and the liquid-vapor interface vanishes. This implies that the ablation mechanisms and hence the entire target treatment need to be revised. Since ablation results in the insertion of matter into the plume above the sample, it can be expected that a change in the ablation mechanism will influence the breakdown process in the plume.

In this work, a model is presented that accounts for the various ablation mechanisms in the target, as well as for the main processes in the plasma. The spatial and temporal evolution of the target is described by a one-dimensional hydrodynamic model, accounting for energy (Eq. (1a)), mass conservation (Eq. (1b)), as well as pressure relaxation (Eq. (1c)):

$$\frac{D\,U(x,t)}{Dt} = \frac{\partial}{\partial x}\kappa(T)\frac{\partial T(x,t)}{\partial x} + S_{\mathrm{las}}(x,t), \tag{1a}$$

$$\frac{D\,\rho(x,t)}{Dt} = -\frac{\partial}{\partial x}\rho(x,t)v(x,t), \tag{1b}$$

$$\frac{D\,P_{\mathrm{m}}(x,t)}{Dt} = -\frac{(P_{\mathrm{m}}(x,t) - P_{\mathrm{pl}})}{\tau_{\mathrm{mech}}(x,t)}. \tag{1c}$$

Here, U, ρ, T, v, κ, and S_{las} denote the internal energy and mass densities, the temperature, the material velocity, the thermal conductivity, and the laser source term, respectively. The sample tends to adjust its pressure P_{m} to the outer plasma pressure P_{pl}, on a time scale characterized by the mechanical relaxation time τ_{mech}.[11,12] The system of equations is closed by a tabulated multiphase equation of state.[13,14] The thermodynamic state of the material and kinetic relations define the acting ablation mechanism. Equations (1a)–(1c) are simultaneously solved in a reference frame attached to the ablating surface. The material derivative D/Dt represents the corresponding coordinate transformation and contains the surface recession velocity v_{r}.

Fig. 1 shows several processes occurring during ns-laser ablation. Three ablation mechanisms can be distinguished: evaporation or condensation (I, v_{ev}), ablation due to bubble growth in the metastable region (II, v_{bub}), and fragmentation in the supercritical region (III, v_{crit}). Hence, the recession velocity can be expressed as $v_{\mathrm{r}}(t) = v_{\mathrm{ev}}(t) + v_{\mathrm{bub}}(t) + v_{\mathrm{crit}}(t)$.[12] A collisional radiative model treats the plasma (see Fig. 1).

a)Electronic mail: dautriqu@physik.uni-kl.de
b)Electronic mail: chenzy@mail.buct.edu.cn

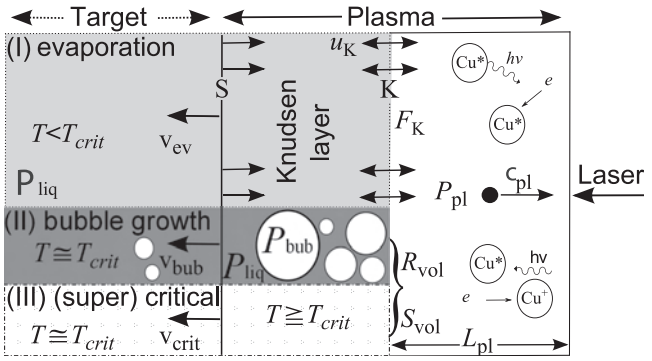

FIG. 1. Schematic representation of target and plasma. Collisional and radiative processes in the plasma are depicted. The plume of length (L_{pl}) expands at the sound speed, c_{pl}. P_{pl}, P_{bub}, and P_{liq} are plasma, bubble, and liquid pressures, respectively. Three ablation mechanisms are shown, starting at the liquid surface (solid line, S). Recession velocities due to evaporation (I, v_{ev}), bubble formation (II, v_{bub}), and (super)critical fragmentation (III, v_{crit}) are indicated. The fluxes F_K and velocity u_K at the end of the Knudsen layer (K) are shown in case I. R_{vol} and S_{vol} express the volumetric particle and energy sources that enter the plasma for cases II and III.

The plasma plume of length L_{pl} is assumed to expand at the sound speed c_{pl}.[7,15,16] Spatial averaging of a system of Euler equations over the plume length, L_{pl}, results in a set of ordinary differential equations, which describes the expanding plume:

$$\frac{dN_i}{dt} = \frac{F_{K,N_i} - F_{pl,N_i}}{L_{pl}} + R_i + R_{vol,i}, \tag{2a}$$

$$\frac{dU_i}{dt} = \frac{F_{K,U_i} - F_{pl,U_i}}{L_{pl}} - P_i \frac{c_{pl} - u_K}{L_{pl}} + S_i + S_{vol,i}, \tag{2b}$$

$$\frac{dL_{pl}}{dt} = c_{pl}. \tag{2c}$$

The species (i = electron and atom) number and internal energy densities are denoted by N_i and U_i, respectively. Since each atom will reside in a certain charge state k excited to level m, N_i should be interpreted as N_m^k in the case of heavy species. The particle and energy fluxes of the species at the end of the Knudsen layer[12,17,18] (F_K) and the plume domain (F_{pl}) are included. The volumetric ablation mechanisms account for the particle (R_{vol}) and energy sources (S_{vol}) of the different species. R_i and S_i denote the particle and energy sources due to the collisional and radiative mechanisms in the plasma.

Collisional processes, such as inverse Bremsstrahlung, electron impact ionization and three body recombination; electron impact excitation and de-excitation; as well as radiative processes, such as photo ionization and recombination, radiative decay and Bremsstrahlung, are included (see Table I).

Note that optical transitions are observed between 352 energy levels in Cu^+.[19] This illustrates that the computational cost would rise tremendously if one would evaluate all optical transitions in copper. Instead, three steps are employed to simplify the model: (1) The maximum considered charge state is 2, i.e., only energy levels up to the ground state of Cu^{2+} are included in the model; (2) only energy levels that participate in the most persistent, optically allowed transitions, are selected; (3) energy levels that belong to similar electron configurations are combined and averaged according to their respective statistical weights. This strategy finally results in 15 copper levels: $Cu_{m=0,\ldots,8}^{k=0}$, $Cu_{m=0,\ldots,4}^{k=1}$ and $Cu_{m=0}^{k=2}$.

TABLE I. Collisional (c) and radiative (r) mechanisms included in the model. The corresponding references, forward, and backward reactions are indicated.

c	Inv. Bremsst.[16,20]	$Cu_m^k + e(\epsilon) + h\nu_{laser} \rightarrow Cu_m^k + e(\epsilon')$
c	Ei. ion./tb.rec.[21–23]	$Cu_m^k + e(\epsilon) \leftrightarrow Cu_n^{k+1} + e(\epsilon') + e(\epsilon'')$
c	Ei. exc./deexc.[23,24]	$Cu_m^k + e(\epsilon) \leftrightarrow Cu_n^k + e(\epsilon')$
r	Phot. ion./rec.[16]	$Cu_m^k + n_{photon}h\nu_{laser} \leftrightarrow Cu_0^{k+1} + e(\epsilon)$
r	Rad. dec.[19,23,25]	$Cu_n^k \rightarrow Cu_m^k + h\nu_{mn}$
r	Bremsst.[16]	$Cu_m^k + e(\epsilon) \rightarrow Cu_m^k + e(\epsilon') + h\nu$

In order to illustrate the influence of the ablation mechanism on the absorption processes in the expanding plume, two calculations are done and compared with the results of a plasma transmission measurement.[26] The first calculation is performed with a commonly employed model, denoted as the "reduced model." Here, only surface mass removal mechanisms are considered: evaporation and condensation. In this case, it is assumed that the equation of state of liquid copper is governed by the liquid-vapor equilibrium line, i.e., the binodal. The liquid part of the binodal starts at the melting point and ends at the critical point. The target cells are assumed to experience a metal-dielectric transition near the critical point and become fully transparent to the incoming laser light when they reach the critical state.[27,28] As a result, the laser light will start to penetrate through the target, and an evaporation front can at all times be attached to the ablating target surface. In the second calculation, the "full model" is employed. Here, both surface and volumetric mass removal mechanisms are considered, whereas no additional assumptions are made with respect to the equation of state or eventual onset of transparency.

Fig. 2(a) shows the calculated temporal evolution of surface temperature (T_S, red) and reflectivity (R_S, black) during the initial ablation stage. Fig. 2(b) interrelates the surface temperature (red) and the calculated laser intensity at the surface (I_a, grey). Also, the experimental laser intensities before (I_o, blue) and after plasma absorption (I_a, blue) are shown. During laser irradiation, the target heats up and the surface temperature rises (see Fig. 2(a)). As a result, the reflectivity decreases[29] and more laser energy couples to the target. As soon as the material exceeds the normal boiling point, evaporation starts. Depending on the employed model, the surface cells will arrive in a thermodynamic state in the vicinity of or at the critical point.

In the reduced model, the critical point is reached at around 8 ns (see Fig. 2(a), dash). At that instant, the material experiences a metal-dielectric transition, becomes transparent, and the reflectivity drops to $R \cong 0.03$.[27] Around 11 ns, the evaporated matter starts to absorb a significant amount of laser light (see Fig. 2(b), grey, dash). Subsequently a hot plasma is formed above the target, which tends to shield the copper sample from the laser beam. As a result, the intensity at the surface decreases. Since the laser light penetrates the transparent, critical target layer, a lot of heat is deposited in the copper sample and the material can be sustained for a while in the critical state. Accordingly, the critical state is

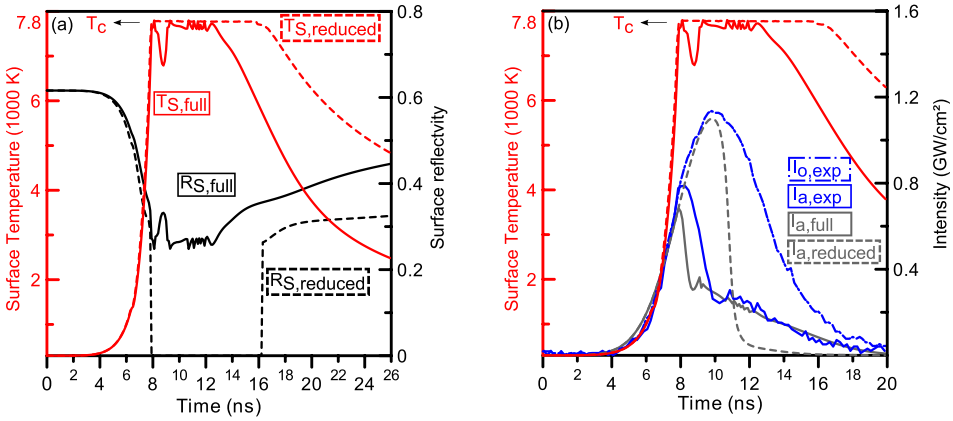

FIG. 2. A 6 ns laser pulse operates at 532 nm and 7.5 J/cm^2. Calculations are done for two cases. The first case considers both surface and volumetric ablation mechanisms (full model, solid), whereas the second case only accounts for surface ablation (reduced model, dash). (a) The temporal evolution of the surface temperature (T_S, red) and reflectivity (R_S, black) is shown. (b) Both the surface temperature and the actual laser intensity at the surface (I_a, grey) are depicted. Besides, the experimental laser profiles before ($I_{o,exp}$, blue, dash-dot) and after plasma absorption ($I_{a,exp}$, blue, solid) are indicated, respectively.

maintained up to 16 ns (see Fig. 2(a), dash), whereas the laser intensity decreases already around 11 ns (see Fig. 2(b), grey, dash). After 16 ns, thermal cooling starts, the surface temperature decreases and the reflectivity increases again.

Contrary to the reduced model, the full model accounts for both evaporation and volumetric ablation mechanisms. The solid lines in Fig. 2(a) represent the corresponding temperature and reflectivity profiles. After evaporation, the material finally arrives in a state close to the critical point. In the metastable liquid state between binodal and spinodal, homogeneous nucleation can result in bubble formation and growth. Eventually, target cells will be converted into a mixture of liquid and gas (see also Fig. 1). Note that this mechanism plays a minor role in the present calculations.[12] Above the critical temperature and density, the copper liquid behaves as a supercritical fluid. In this state, the material cannot sustain its surface tension and the target fragments. As a result, a lot of material will be removed in a short time from the target. The laser triggers breakdown in the ablated material, followed by plasma absorption. As a result, a decrease of the surface temperature and hence an increase of the reflectivity around 8 ns are observed. Subsequently, the dense plasma above the sample will tend to expand, whereas its density decreases. Correspondingly, the laser irradiance at the surface rises again around 9 ns in Fig. 2(b) (grey, solid), whereas the surface temperature reestablishes its critical value around 9 ns. Every time a surface cell arrives in the supercritical region, fragmentation results in an increase of the plume density and hence an increase of plasma absorption. As a result, a fine structure in the intensity profile is observed around 11 ns. Afterwards, around 13 ns, cooling starts: the surface temperature now decreases, whereas the reflectivity increases again.

A comparison between the calculated intensity profiles at the surface reveals that their shapes are quite different (see Fig. 2(b)). Besides, the full model exhibits a fine structure, whereas the reduced model does not. Moreover, the onset of shielding occurs 3 ns later in the reduced model, contrary to the full model and the experiment. Hence, this indicates that the plasma responds differently when the ablation mechanism changes. Overall, one observes that the pattern produced by the full model matches well with the experiment.

Fig. 3 displays the temporal evolution of the species temperatures in the two models. Besides, a temperature estimate is inserted, assuming Saha-Boltzmann distributed atomic states (T_{LSBE}, blue). The inset in Fig. 3 shows that a non-equilibrium plasma is initially encountered in both models. During volumetric ablation, the electrons will frequently collide with the heavy species. Hence, contrary to the reduced model, the full model achieves already during the early ablation stage a state close to LSBE and the onset of shielding starts earlier ($\Delta t_{shield} = 3$ ns). At later times, a two temperature LSBE plasma is found in both models. After the end of the laser pulse, a Maxwell equilibrium is almost established and a state near Local Thermodynamic Equilibrium (LTE) is met. Afterwards, as the plume expands, its density decreases and the species experience fewer collisions. As a result, the species temperatures differ again in both models.

Fig. 4 shows the plasma absorption coefficients at $\lambda = 532$ nm. In both cases, breakdown starts with the generation of free electrons by single and multi-photon ionization. Afterwards, collisions become increasingly important, and inverse Bremsstrahlung absorption is observed: first, electrons absorb laser energy in the electric field of neutrals; finally, electron-ion inverse Bremsstrahlung starts. In short,

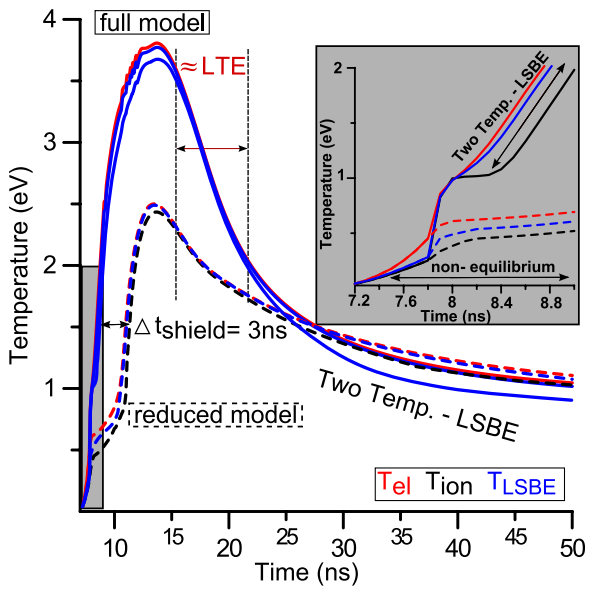

FIG. 3. The evolution of the electron (T_{el}, red) and ion (T_{ion}, black) temperatures is shown for both models. The subfigure illustrates the situation when ablation starts. T_{LSBE} (blue) is a temperature estimate, assuming Saha-Boltzmann distributed atomic states.

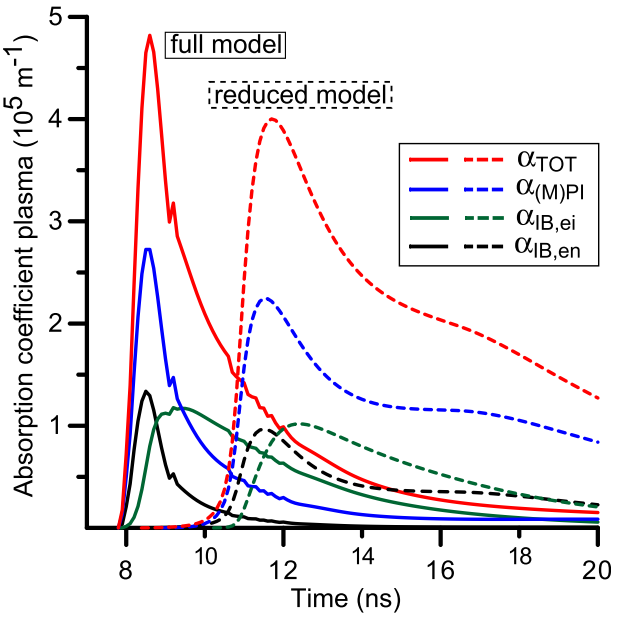

FIG. 4. The total (α_{TOT}, red) and partial plasma absorption coefficients due to electron-neutral ($\alpha_{IB,en}$, black), electron-ion ($\alpha_{IB,ei}$, green) inverse Bremsstrahlung, and photo ionization ($\alpha_{(M)PI}$, blue) at $\lambda = 532$ nm are depicted, respectively.

the calculations illustrate that photo-ionization[8,9] and not inverse Bremsstrahlung[30] initially predominates during UV-VIS laser irradiation, whereas the plasma should rather be modelled by a 2T-LSBE model and not by a LTE model.[30–32]

In Fig. 5, calculated (black) and experimental (blue) transmissivities of laser light are compared. Note that the experiment is conducted in argon at atmospheric pressure,[26,32] whereas the calculations assume a vacuum. Nevertheless, the influence of argon on the transmission profiles can be neglected: as the copper plasma acquires a large amount of thermal energy initially, the region between the contact discontinuity and the external shock front will play a minor role during the initial expansion stage.[1,32] When both

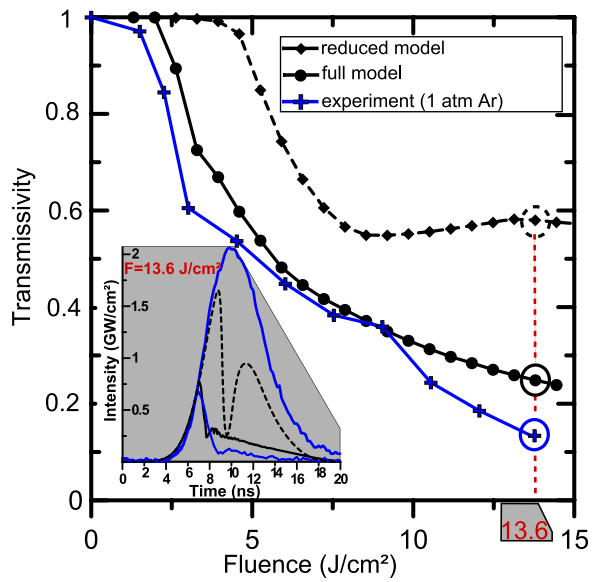

FIG. 5. Calculated and experimental transmissivities vs fluence are shown for $\lambda = 532$ nm. The subfigure depicts temporal intensity profiles, taken at 13.6 J/cm^2.

surface and volumetric ablation mechanisms are included (full model), a good agreement between experiment (blue) and theory (solid, circles) is obtained. However, if only surface ablation is considered (reduced model), the calculated profile (dash, diamonds) deviates considerably from the experimental one. While the experimental breakdown threshold is around 2 J/cm^2, the reduced model shows a threshold around 5 J/cm^2. Moreover, the transmissivities tend to saturate above a fluence F = 8 J/cm^2.

The inset in Fig. 5 shows a temporal intensity profile taken at a fluence F = 13.6 J/cm^2. Contrary to the multiphase model and the experiment, the reduced model (dash) exhibits a clear bimodal pattern in its intensity profile. In this case, the plume experiences a significant density decrease during expansion, and the laser intensity at the target surface rises. This effect was systematically observed for fluences above F = 8 J/cm^2. In this fluence range, the intensity patterns are characterized by similar integrals and hence similar transmissivities. This illustrates again that the ablation mechanism affects the plasma response strongly.

In conclusion, a dimensionless multiphase collisional radiative model describing ns-laser ablation has been presented. Initially, a non-equilibrium plasma is formed and photo-ionization predominates. Afterwards, collisional ionization starts and a two-temperature LSBE plasma is observed. It is found that the plasma responds differently to the various ablation mechanisms. In the multiphase model, both surface and volumetric ablation mechanisms are included, and a good agreement with the experiment is achieved. However, if only surface ablation is considered, the plasma response changes and a serious mismatch between calculations and experiment is observed. This demonstrates that a multiphase approach is indispensable in the computational study of ns-laser ablation.[33,34]

The authors wish to thank O. Rosmej for her valuable comments and efforts. G. Clair and D. L'Hermite are acknowledged for providing the experimental data. David Autrique thanks J.J.A.M. van der Mullen for the interesting suggestions. Financial support from the Deutsche Forschungsgemeinschaft (Emmy Noether-Program, grant RE 1141/11) is acknowledged.

[1]D. Bäuerle, *Laser Processing and Chemistry* (Springer-Verlag, Berlin, 2011), pp. 3–851.
[2]G. M. Weyl, "Physics of laser-induced breakdown: An update," in *Laser-Induced Plasmas and Applications*, edited by L. Radziemski and D. Cremers (Marcel Dekker, New York, 1989), pp. 1–67.
[3]J. Van der Mullen, Phys. Rep. **191**, 109 (1990).
[4]M. Capitelli, F. Capitelli, and A. Eletskii, Spectrochim. Acta, Part B **55**, 559 (2000).
[5]I. B. Gornushkin and U. Panne, Spectrochim. Acta, Part B **65**, 345 (2010).
[6]V. Mazhukin, I. Gusev, I. Smurov, and G. Flamant, Appl. Surf. Sci. **96–98**, 82 (1996).
[7]S. Amoruso, Appl. Phys. A: Mater. Sci. Process. **69**, 323 (1999).
[8]V. Morel, A. Bultel, and B. Chéron, Spectrochim. Acta, Part B **65**, 830 (2010).
[9]V. Mazhukin, V. Nossov, M. Nikiforov, and I. Smurov, J. Appl. Phys. **93**, 56 (2003).
[10]L. Pietanza, G. Colonna, A. D. Giacomo, and M. Capitelli, Spectrochim. Acta, Part B **65**, 616 (2010).
[11]B. Chimier, V. Tikhonchuk, and L. Hallo, Appl. Phys. A: Mater. Sci. Process. **92**, 843 (2008).

[12]D. Autrique, G. Clair, D. L'Hermite, V. Alexiades, A. Bogaerts, and B. Rethfeld, J. Appl. Phys. **114**, 023301 (2013).
[13]A. V. Bushman, G. I. Kanel', L. A. Ni, and V. E. Fortov, *Intense Dynamic Loading of Condensed Matter* (Taylor & Francis, Washington, 1993), pp. 116–145.
[14]P. R. Levashov and K. V. Khishchenko, *ITTEOS 5.8 Software for Calculation of EOS for Metals* (Institute for High Energy Densities, Moscow, Russia, 2007).
[15]S. I. Anisimov, *Instabilities in Laser-Matter Interaction* (CRC Press, Boca Raton, 1995), pp. 45–56.
[16]B. Zel'dovich and Y. P. Raizer, *Physics of Shock Waves and High-Temperature Hydrodynamic Phenomena* (Dover, New York, 2002), Vols. 1 and 2, pp. 192–292.
[17]S. I. Anisimov, Sov. Phys. JETP **27**, 182 (1968).
[18]C. J. Knight, AIAA J. **17**, 519 (1979).
[19]Y. Ralchenko, A. Kramida, J. Reader, and NIST ASD team, NIST Atomic Spectra Database (Version 3.1. 5), 2008.
[20]Y. B. Zel'dovich and Y. P. Raizer, Sov. Phys. JETP **20**, 772 (1965).
[21]W. Lotz, Z. Physik **216**, 241 (1968).
[22]W. Lotz, Z. Physik **232**, 101 (1970).
[23]H. Chung, M. Chen, W. Morgan, Y. Ralchenko, and R. Lee, High Energy Density Phys. **1**, 3 (2005).
[24]H. van Regemorter, Astrophys. J. **136**, 906 (1962).
[25]R. Kurucz and B. Bell, Atomic Line Data, CD-ROM No. 23, 1995.
[26]G. Clair, "Etudes théorique et expérimentale des plasmas produits par laser en vue de leur application à l'analyse chimique des matériaux en environment complexe," Ph.D. dissertation (Université d'Aix-Marseille II, 2011).
[27]V. Batanov, F. Bunkin, A. Prokhorov, and V. Fedorov, Sov. Phys. JETP **36**, 311 (1973).
[28]J. H. Yoo, S. H. Jeong, R. Greif, and R. E. Russo, J. Appl. Phys. **88**, 1638 (2000).
[29]A. Prokhorov, V. Konov, I. Ursu, and I. N. Mihailescu, *Laser Heating of Metals* (Adam Hilger, Bristol, 1990), pp. 1–30.
[30]A. Bogaerts and Z. Chen, Spectrochim. Acta, Part B **60**, 1280 (2005).
[31]M. Aghaei, S. Mehrabian, and S. H. Tavassoli, J. Appl. Phys. **104**, 053303 (2008).
[32]G. Clair and D. L'Hermite, J. Appl. Phys. **110**, 083307 (2011).
[33]S. Anisimov and B. Luk'yanchuk, Phys. Usp. **45**, 293 (2002).
[34]M. S. Qaisar and G. J. Pert, J. Appl. Phys. **94**, 1468 (2003).